International Journal of Multiphase Flow 171 (2024) 104697

Contents lists available at ScienceDirect

International Journal of Multiphase Flow

journal homepage: www.elsevier.com/locate/ijmulflow

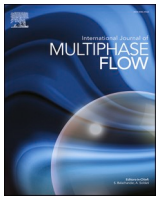

Numerical simulations of a compact inline gas–liquid separator: A comparison between RANS and a hybrid LES-RANS approach

Francesco Maluta *, Alessandro Paglianti, Giuseppina Montante

Dipartimento di Chimica Industriale 'Toso Montanari', Alma Mater Studiorum – Università di Bologna, Viale del Risorgimento 4, 40136 Bologna, Italy

ARTICLE INFO

Keywords:
Detached Eddy simulation
Gas–liquid flow
Inline separator
CFD
PBE

ABSTRACT

Two computational fluid dynamics approaches are adopted to simulate the single-phase and the gas–liquid flow field generated by a compact inline separator based on the generation of a swirling flow. The results of a detached eddy simulation, DES, combining a large eddy approach with the realizable k-ε turbulence model were compared to RANS results and experimental data from the literature. The DES better replicates the experimentally observed velocity fluctuations, pressure drop, gas distribution and gas–liquid separation profiles, with respect to the RANS approach. A population balance equation was solved in the flow fields produced by the two simulation approaches, and important differences were found in the mean bubble characteristic diameter spatial distributions, possibly due to the different predictions of the local values of turbulent dissipation rates, which affect the bubble breakup and coalescence phenomena.

1. Introduction

Gas–liquid separation based on swirling flows relies on the generation of a rotating flow producing angular accelerations larger than the gravitational one, thus enhancing the separation characteristic times, based on phase density difference, and resulting in smaller equipment (Bird et al., 1960). Since this technique can reduce the overall impact of the equipment, it is compliant with the principles of process intensification (Stankiewicz and Moulijn, 2000). Moreover, this separation technique is commonly adopted in a large variety of engineering applications, such as centrifuges, cyclones, and inline separators (Green and Perry, 2008). In particular, the adoption of gas–liquid separator devices based on swirling flow operating inside pipes, also called inline swirling devices, is particularly promising and it is currently adopted in industrial operations especially related to energy production (Kharoua et al., 2018; Yin et al., 2016; Zhang et al., 2020).

The Computational Fluid Dynamics, CFD, modeling of such systems is generally based on the robust and widespread Reynolds Averaged Navier–Stokes (RANS) approach (Coroneo et al., 2012; Maluta et al., 2023; Song et al., 2021). The modeling effort was firstly directed towards very diluted gas–liquid systems (Cai et al., 2014), and it was successively extended to higher gas flow rates with limited interphase interactions (Zidouni et al., 2015) and monodispersed bubble sizes (Putra et al., 2018). Recently, the CFD simulation of such devices was coupled with the solution of a population balance equation, PBE, to describe the different sizes of the bubble population (Maluta et al., 2023; Yuan et al., 2020). Some open issues highlighted in a previous publication are related to the shape and position of the central zone where the gas accumulates, as well as the description of the turbulent and fluctuating flow fields which in turns also affect the bubble breakup and coalescence phenomena (Maluta et al., 2023).

These aspects may be related to the intrinsic limitations of the RANS modeling approach, which transports just the mean velocity components, while modeling the fluctuating velocity components (Versteeg and Malalasekera, 2007). Conversely, a different approach requires the solution of all the fluid flow scales, from the integral down to the dissipative ones, but while the direct numerical simulation, DNS, increases the accuracy of the predictions, it greatly increases the computational costs, and its adoption in multiphase equipment simulation is still limited. Between these two extremes, large eddy simulations, LES, have been commonly used in modeling gas–liquid and multiphase equipment for chemical engineering applications. For instance, LES simulations were employed in the separation of solid particles from a gas stream in swirling cyclones (Derksen et al., 2008) and solid-liquid systems were studied with an Euler-Euler approach (Guha et al., 2008). Concerning gas–liquid applications, bubble columns were extensively modeled with LES approaches in the last 20 years (Deen et al., 2001), with recent advanced applications coupling PBEs in solutions with

* Corresponding author.
E-mail address: francesco.maluta@unibo.it (F. Maluta).

https://doi.org/10.1016/j.ijmultiphaseflow.2023.104697
Received 26 July 2023; Received in revised form 13 November 2023; Accepted 8 December 2023
Available online 16 December 2023

anionic surfactants (Kouzbour et al., 2023). Besides the bubble column example, different LES applications to bubbly flows are found in the literature, and a review is available on the topic (Dhotre et al., 2013). On the other hand, wall-bounded applications with complex geometries and internals require fine grid resolutions at the walls which increase the computational times, thus limiting the adoption of the LES approach. A solution is found by using hybrid LES-RANS approaches which use the RANS formulation of the fluid flow equations near the walls, while recovering the LES formulations in the free stream (Spalart et al., 2006). These hybrid approaches have been used in the simulation of single-phase process equipment such as stirred tanks (Gimbun et al., 2012) and draft tube reactors (Brown et al., 2020), for instance, but their application to multiphase and especially gas–liquid systems is still limited.

One of the first gas–liquid applications of these hybrid RANS-LES approaches is found in the numerical simulation of a hydraulic jump, where the two-fluid model is coupled with a detached eddy simulation, DES, using the baseline k-ω turbulence model as sub-grid model and close to the walls (Ma et al., 2011), and it was later adopted to validate the prediction of the bubble entrainment (Wang et al., 2019). A similar Euler-Euler approach, but with the k-ω SST turbulence model for the solution of the DES equations in RANS mode was applied to bubble columns (Masood and Delgado, 2014). A successive study analyzed different turbulence models for the RANS operation of the hybrid RANS-LES approaches in bubble columns (Masterov et al., 2018), with a two-way Lagrangian direct simulation Monte Carlo description of the bubbles. Detached Eddy Simulation with the Spalart-Allmaras turbulence model was employed in the numerical simulations of Taylor bubbles rising in a stagnant liquid with the volume of fluid model. The modeling approach allowed the study of velocity and gas volume fraction profiles, as well as the interphase heat transfer due to the wall heating and the coalescence mechanism of two bubbles (Shaban and Tavoularis, 2018). The DES approach was also recently adopted, in conjunction with the algebraic slip mixture model, in the simulation of the flow of cryogenic liquid oxygen through the nozzle of the lower-stage boosters in the rocket engines realizing lift off (Lyras et al., 2021). These variety of applications show that the DES approach can be coupled with different multiphase models, such as Eulerian, Lagrangian and mixture models.

In this work, the DES approach was applied to the numerical simulation of a compact inline swirling device for gas–liquid separation operating in a horizontal pipe, and the predictions are compared with RANS simulations results and experimental measurements from a previous study (Maluta et al., 2023). The manuscript is organized as follows: the system and the investigated operative conditions are firstly shown. Successively, the computational model is presented, starting from the equations governing the gas liquid flow, then reporting the turbulence model and the population balance equation. The numerical solution strategy is then described, followed by single-phase results, gas–liquid simulations, and the results of the solution of the population balance equation. Finally, conclusions are drawn.

2. System and operative conditions

A compact inline separator, called swirler for short, consisting of a central cylindrical hub of diameter 25 mm from which six 2 mm thick flat blades tilted 45° from the hub axis was coaxially positioned inside a horizontal 90 mm diameter pipe. The swirler blades extended up to the pipe walls, the pipe inlet and outlet were positioned 900 mm before and after the swirler, respectively, and the total axial length of the swirler was 13 mm. The swirler geometry inside the pipe is reported in Fig. 1.

Single phase simulations were performed with the fluid properties of tap water at 25°C, with the fluid density being $\rho_L = 998$ kg/m^3, its viscosity being $\mu_L = 0.001$ Pa s, and the total volume flow rate being 20 m^3/h. Gas–liquid simulations were performed adding a gas phase consisting of air, which density is $\rho_G = 1.225$ kg/m^3, to the tap water liquid phase. In this case the liquid volume flow rate was equal to 25 m^3/h and the gas volume flow rate was equal to 7.5 L/min.

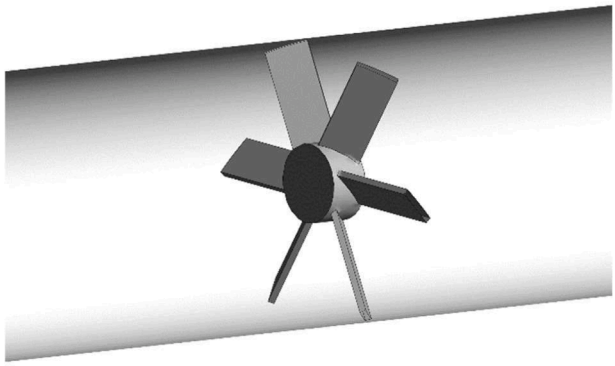

Fig. 1. Cutaway drawing of the swirler geometry inside the pipe.

The geometry and the operative conditions considered match those reported in a previous work (Maluta et al., 2023). The experimental results reported there were adopted to validate the results of the numerical simulations. In particular the liquid phase fluctuating velocity profiles, the pressure drop and the gas-phase distribution in the pipe downstream the swirler as predicted by the numerical simulations were compared with the experimental data.

3. Computational model

In this Section the set of equations solved to model the flow in the system described in Section 2 is presented. Firstly, the equations describing gas–liquid flow are presented, successively the RANS and hybrid LES/RANS approaches are presented, and ultimately the population balance equation is reported.

3.1. Flow equations

The description of the fluid flow started from the incompressible, isothermal Navier–Stokes equations, written for a fluid with phase averaged mixture properties:

$$\frac{\partial \rho_m}{\partial t} + \frac{\partial \rho_m u_i^m}{\partial x_i} = 0 \tag{1}$$

$$\frac{\partial \rho_m u_i^m}{\partial t} + \frac{\partial}{\partial x_j}\left(\rho_m u_i^m u_j^m\right) = -\frac{\partial p}{\partial x_i} + \frac{\partial}{\partial x_j}\left(\mu_m\left(\frac{\partial u_i^m}{\partial x_j} + \frac{\partial u_j^m}{\partial x_i}\right)\right) + \rho_m g + \frac{\partial}{\partial x_j}\tau_{ij}^{Mod.} - \frac{\partial}{\partial x_j}\left(\alpha_G \rho_G v_i^{d,G} v_j^{d,G} + \alpha_L \rho_L v_i^{d,L} v_j^{d,L}\right) \tag{2}$$

$$\frac{\partial}{\partial t}\left(\alpha_G \rho_G\right) + \frac{\partial}{\partial x_i}\left(\alpha_G \rho_G u_i^m\right) = -\frac{\partial}{\partial x_i}\left(\alpha_G \rho_G v_i^{d,G}\right) \tag{3}$$

Where in the continuity equation, Eq. (1), ρ_m is the density of the mixture, u_i^m is the $i-th$ component of the mixture fluid velocity, and in the momentum conservation equation, Eq. (2), p is the pressure, μ_m is the mixture dynamic viscosity, g is the gravitational acceleration, $\tau_{ij}^{Mod.}$ is a stress tensor which needs to be modeled, and the last term represents a contribution accounting for the velocities of the individual gas and liquid phases. This last term depends on the gas phase (subscript G) and on the liquid phase (subscript L) volume fractions, α, densities, ρ, and drift velocities v_i^d. Eq. (3) is a transport equation for the gas phase volume fraction.

The phase average mixture properties are obtained from the individual phase properties through the following mixing relationships:

$$\rho_m = \alpha_G \rho_G + \alpha_L \rho_L \tag{4}$$

$$\mu_m = \alpha_G \mu_G + \alpha_L \mu_L \tag{5}$$

$$u_i^m = \frac{\alpha_G \rho_G u_i^G + \alpha_L \rho_L u_i^L}{\alpha_G \rho_G + \alpha_L \rho_L} \tag{6}$$

The drift velocities in Eqs. (2) and (3) are obtained from the individual phase velocities as:

$$v_i^{d,G} = \left(1 - \frac{\alpha_G \rho_G}{\rho_m}\right) u_i^{GL} \tag{7}$$

$$v_i^{d,L} = -\left(1 - \frac{\alpha_L \rho_L}{\rho_m}\right) u_i^{GL} \tag{8}$$

Where the term u_i^{GL} is the gas–liquid slip velocity, which is the difference between the gas-phase velocity and the liquid-phase velocity. To obtain this term, an algebraic equation is adopted (Manninen et al., 1996), which accounts for the interphase drag and the interphase turbulent dispersion, and it reads as:

$$u_i^{GL} = \frac{4}{3}\frac{\rho_G - \rho_m}{\rho_L}\frac{d_B}{|u^{GL}|C_D}\left(g - u_i^m\frac{\partial u_j^m}{\partial x_i} - \frac{\partial u_i^m}{\partial t}\right) - \frac{\eta_t}{\sigma_t}\left(\frac{1}{\alpha_G}\frac{\partial \alpha_G}{\partial x_i} - \frac{1}{\alpha_L}\frac{\partial \alpha_L}{\partial x_i}\right) \tag{9}$$

With d_B being the bubble size, C_D being the drag coefficient, η_t being the turbulent diffusivity and σ_t being the turbulent Schmidt number equal to 0.75. The turbulent diffusivity is calculated from the continuous-dispersed fluctuating velocity correlation, assuming the following form:

$$\eta_t = \frac{\mu_t}{\rho_L}\left[1 + \left(1.8 - 1.35\left(\frac{v_i^{GL}u_i^G}{|v^{GL}||u^G|}\right)^2\right)\left(\frac{|v^{GL}|}{\sqrt{2/3k}}\right)^2\right]^{-\frac{1}{2}} \tag{10}$$

With μ_t being the turbulent viscosity and k being the turbulent kinetic energy. To close Eq. (9), either a constant d_B must be provided or a PBE must be solved, and in this work both approaches were investigated. Moreover, the drag coefficient was obtained from the model developed by Ishii and Zuber (Ishii and Zuber, 1979), which allows to account for the varying bubble shape on the gas–liquid drag, defined as:

$$C_D = \max\left(C_D^{sphere}, \min\left(C_D^{ellipse}, C_D^{cap}\right)\right), \begin{cases} C_D^{sphere} = \frac{24}{Re_B}\left(1 + 0.15Re_B^{0.687}\right) \\ C_D^{ellipse} = \frac{2}{3}\sqrt{Eo} \\ C_D^{cap} = \frac{8}{3} \end{cases} \tag{11}$$

Where $Re_B = |v^{GL}|\rho_L d_B/\mu_L$ is the bubble Reynolds number, and $Eo = g(\rho_L - \rho_G)d_B^2/\sigma$ is the Eötvös number, which depends on the gas–liquid surface tension, σ, assumed as constant and equal to 0.072 N/m. The bubble swarm effect on the interphase forces was neglected and the drag force formulation for dilute systems is adopted, as previously done for the RANS simulation of similar systems (Putra et al., 2018). The thorough analysis of the effect of a three-way coupling on the interphase interaction forces may be the topic for future studies.

In Eq. (2), the term $\tau_{ij}^{Mod.}$ is a stress tensor and, depending on the turbulence modeling approach, $\tau_{ij}^{Mod.}$ can alternatively be interpreted either as the Reynolds stress tensor, in case of a RANS approach, or the sub-filter stress tensor when the LES approach is employed. The description of this term is presented in Section 3.2.

3.2. Turbulence modeling

The modeled stress tensor in Eq. (2) is described through the Boussinesq approximation, which results in:

$$\tau^{Modelled} = \frac{\mu_t}{\rho_m}\left(\frac{\partial u_i}{\partial x_j} + \frac{\partial u_j}{\partial x_i}\right) \tag{12}$$

To calculate the turbulent viscosity two different approaches were adopted. With the RANS approach, the two equation realizable k-ε model (Shih et al., 1995) was adopted to transport the turbulent kinetic energy, k, and its dissipation, ε:

$$\frac{\partial}{\partial t}(\rho_m k) + \frac{\partial}{\partial x_j}\left(\rho_m k u_j^m\right) = \frac{\partial}{\partial x_j}\left[\left(\mu_m + \frac{\mu_t}{\sigma_k}\right)\frac{\partial k}{\partial x_j}\right] + G_k - \rho_m \varepsilon \tag{13}$$

$$\frac{\partial}{\partial t}(\rho_m \varepsilon) + \frac{\partial}{\partial x_j}\left(\rho_m \varepsilon u_j^m\right) = \frac{\partial}{\partial x_j}\left[\left(\mu_m + \frac{\mu_t}{\sigma_\varepsilon}\right)\frac{\partial \varepsilon}{\partial x_j}\right] + \rho_m C_1 S\varepsilon - \rho_m C_2 \frac{\varepsilon^2}{k + \sqrt{\nu_m \varepsilon}} \tag{14}$$

Where $\sigma_k = 1.0$, $\sigma_\varepsilon = 1.2$, $C_1 = \max\left(0.43, \frac{Sk/\varepsilon}{Sk/\varepsilon + 5}\right)$ and $C_2 = 1.9$ are model constants, $G_k = \mu_t S^2$ is the term accounting for the production of k, and S is the rate of strain magnitude. From k and ε the turbulent viscosity is calculated as:

$$\mu_t = \rho C_\mu \frac{k^2}{\varepsilon} \tag{15}$$

With C_μ being a model constant that depends on the rate of strain tensor, S_{ij}, and on the mean rate of rotation tensor, $\tilde{\Omega}_{ij}$:

$$C_\mu = \frac{1}{A_0 + A_S\frac{k}{\varepsilon}\sqrt{S_{ij}S_{ij} + \tilde{\Omega}_{ij}\tilde{\Omega}_{ij}}} \tag{16}$$

With $A_0 = 4.04$ and A_S dependent on the strain rate tensor as:

$$A_S = \sqrt{6}\cos^{-1}\left(\frac{1}{3}\cos^{-1}\left(\sqrt{6}\,\frac{S_{ij}S_{jk}S_{ki}}{\sqrt{S_{ij}S_{ij}}^3}\right)\right) \tag{17}$$

The realizable k-ε model was adopted since previous RANS simulations on the same system highlighted that with the standard k-ε model a better agreement with the experimental data was observed, compared to k-ω and Reynolds Stress Model simulations (Maluta et al., 2023). Since where the flow features include strong streamline curvature and rotation the realizable k-ε model is expected to improve the predictions of the standard k-ε model (Shih et al., 1995), the former model was employed in this work.

The stress tensor in Eq. (12) was also modeled with a LES approach, and in particular, a Delayed Detached Eddy Simulation with the realizable k-ε model was employed. With this approach, the dissipation term in Eq. (13) for the transport of turbulent kinetic energy is modified as:

$$\frac{\partial}{\partial t}(\rho_m k) + \frac{\partial}{\partial x_j}\left(\rho_m k u_j^m\right) = \frac{\partial}{\partial x_j}\left[\left(\mu_m + \frac{\mu_t}{\sigma_k}\right)\frac{\partial k}{\partial x_j}\right] + G_k - \frac{\rho_m k^{\frac{3}{2}}}{l_{DES}} \tag{18}$$

With the term l_{DES} being a modified mixing length for delayed DES which reads as:

$$l_{DES} = \frac{k^{\frac{3}{2}}}{\varepsilon} - f_d \max\left(0, \frac{k^{\frac{3}{2}}}{\varepsilon} - C_{DES}\Delta\right) \tag{19}$$

Where $C_{DES} = 0.61$ is a calibration constant analog to the Smagorinsky constant and f_d is the so-called DES turbulent kinetic energy dissipation multiplier. Δ is the grid size, which is the cell maximum side length. Since the dissipation term in the transport equation depends on the grid size, the DES approach behaves either like LES simulation or as a RANS simulation depending on the cell distance from the wall, d_w. In fact, the term f_d is defined as:

$$f_d = 1 - \tanh\left(\left(20\frac{\nu_t+\nu}{\sqrt{\frac{\partial u_i}{\partial x_j}\frac{\partial u_i}{\partial x_j}}\kappa^2 d_w^2}\right)^3\right) \tag{20}$$

With κ being the von Kármán constant equal to 0.41. Away from the walls, f_d approaches 1 and Eq. (18) moves towards a LES-like model, while close to the walls it recovers its RANS formulation.

3.3. Population balance equation

In section 3.1 Eq. (9) was presented and it was stated that either a constant d_B or a PBE must be solved to close it. The constant bubble size was taken from experimental observation performed in the pipe section downstream of the swirler close to the pipe walls (Maluta et al., 2023), and it was equal to 1.40 mm, while the PBE solved to obtain the bubble population size is presented hereafter. The bubble size number density function, $n(d)$, transport equation reads as

$$\frac{\partial n(d)}{\partial t} + \frac{\partial}{\partial x_i}\left(u_i^G n(d)\right) = B^{Br} + B^C - D^{Br} - D^C \tag{21}$$

Where the source terms on the right-hand-side of Eq. (21) account for the bubble birth, B, and death, D, due to coalescence, C, and breakup, Br, phenomena.

The discrete source terms due to coalescence in Eq. (21) are expressed as:

$$B^C - D^C = \frac{1}{2}\int_0^d a\left(\left(d^3-\delta_B^3\right)^{\frac{1}{3}},\delta_B\right)n\left(\left(d^3-\delta_B^3\right)^{\frac{1}{3}}\right)n(\delta_B)d\delta_B - n(d)\int_0^\infty a(d,\delta_B)n(\delta_B)d\delta_B \tag{22}$$

With $a(d,\delta_B)$ being the aggregation kernel, described with the model by Prince and Blanch (Prince and Blanch, 1990), and it reads as:

$$a(d,\delta_B) = \frac{\pi\sqrt{2}}{4}\varepsilon^{\frac{1}{3}}(d+\delta_B)^2\left(d^{\frac{2}{3}}+\delta_B^{\frac{2}{3}}\right)^{\frac{1}{2}}\exp\left(-\gamma\frac{\varepsilon^{\frac{1}{3}}\rho_L^{\frac{1}{2}}}{\sigma^{\frac{1}{2}}}\left(\frac{1}{d}+\frac{1}{\delta_B}\right)^{-\frac{5}{6}}\right) \tag{23}$$

The kernel is obtained assuming that bubble collisions are dominated by turbulence fluctuations in an isotropic turbulence field. The exponential in Eq. (23) expresses the coalescence efficiency. The model constant γ is equal to 1.7 and it holds information on the initial and final liquid film thickness between the two coalescing bubbles, which values are assumed equal to those in the original work by Prince and Blanch.

The discrete source terms due to breakup effects in Eq. (21) are:

$$B^{Br} - D^{Br} = \int_{d_B}^\infty \frac{\Omega(d,\delta_B)}{n(d)}n(d)d\delta_B - b(d)n(d) \tag{24}$$

Where d is the parent bubble and δ_B is the child. The total breakup frequency function, Ω/n, is obtained through the breakup kernel developed by Luo and Svendsen (Luo and Svendsen, 1996) and binary breakage occurs due to the energy of the colliding eddies exceeding a threshold value. The frequency function reads as:

$$\frac{\Omega(d,\delta_B)}{n(d)} = 0.923(1-\alpha_G)\left(\frac{\varepsilon}{d^2}\right)^{1/3}\int_{\zeta_{min}}^1 \frac{(1+\zeta)^2}{\zeta^{\frac{11}{3}}}\exp\left(\frac{-12c_f(d,\delta_B)\sigma}{\beta\rho_L\varepsilon^{\frac{2}{3}}d^{\frac{5}{3}}\zeta^{\frac{11}{3}}}\right)d\zeta \tag{25}$$

With ζ being the non-dimensional eddy size, the lower limit of integration being $\zeta_{min} = 11.4(\mu_L/\rho_L)^{3/4}/(\varepsilon^{1/4}d)$, β being the model constant equal to 2.045 and $c_f(d,\delta_B)$ being the surface energy increase constraint defined as:

$$c_f(d,\delta_B) = \left(\frac{d^3}{\delta_B^3}\right)^{\frac{2}{3}} + \left(1-\frac{d^3}{\delta_B^3}\right)^{\frac{2}{3}} - 1 \tag{26}$$

Several breakup and coalescence kernels exist in the literature, with different levels of approximations and describing different mechanisms. The present choice of the breakup and coalescence kernels is mostly driven by the widespread adoption of such kernels, by their relative simplicity of implementation and by the reduced computational cost. Future work may investigate different breakup and coalescence mechanisms and implementations.

The present PBE was solved with the quadrature method of moments (QMOM) (Buffo et al., 2016; Falzone et al., 2018; Marchisio and Fox, 2013) by applying the moment transform to Eq. (21). The moment of order k, M_k, was estimated with a quadrature approximation of order N_Q as:

$$M_k = \int_0^\infty n(d)d^k dd \approx \sum_{i=0}^{N_Q} w_i\xi_i^k \tag{27}$$

Where the quadrature weights, w, and abscissas, ξ, are obtained from the transported moments with the Product-Difference algorithm. In this work a quadrature approximation of order 3 was employed, by transporting the first six moments of the bubble number density function.

The method of moments is particularly computationally efficient in obtaining the bubble size for the interphase forces. In fact, when the PBE is solved, the Sauter mean diameter is employed as the bubble size in Eq. (9), which is readily obtained as the ratio of the moment of order 3 over the moment of order 2, without the need to reconstruct the NDF each iteration (Marchisio and Fox, 2013).

4. Numerical solution

4.1. Computational grid

The grid was selected following a convergence study in single-phase conditions, performed on three different grids. The grids consisted almost entirely of hexahedral cells, while just in the volume in the close proximity of the swirler tetrahedral cells were used. The intermediate mesh was obtained by doubling the number of nodes of the coarsest grid in each coordinate, and similarly the finest grid was obtained by doubling the nodes of the intermediate grid. The coarsest grid consists of around 200'000 cells, the intermediate grid consists of around 1.5 million cells and the finest grid of around 11.6 million cells. The corresponding linear resolution is 1.6 mm, 1.0 mm and 0.5 mm for the coarsest, intermediate, and finest grid, respectively, and the angular resolutions is 6°, 3° and 1.5°. The resulting y^+ values ranged between 1 and 80 for the coarsest mesh and between 0.8 and 60 for the finest mesh. In the finest mesh, 99 % of the cells have a y^+ value lower than 30, which is a typical value for DES simulations (Brown et al., 2020), with just a few cells on the edge of the swirler blades with higher y^+ values. For the realizable k-ε model, a near-wall modeling method blending the linear and logarithmic sublayer formulations of the law-of-the-wall was adopted, thus ensuring the correct asymptotic behavior for large and small values of y^+, and reasonable representation of velocity profiles in the wall buffer region, y^+ between 3 and 10 (Kader, 1981).

In order to resolve the large eddies with size in the order of the integral length-scale, Lt, the mesh size must be smaller than 5 Lt, and ideally smaller than 10 Lt (Brown et al., 2020). The integral length-scale is defined as (Marshall and Bakker, 2004):

$$Lt = k^{\frac{3}{2}}/\varepsilon \tag{28}$$

And the ratio Lt/Δ obtained from RANS simulations with the three different computational grids is shown in Fig. 2.

Fig. 2 shows that the coarsest mesh, Fig. 2a, is not fine enough for the

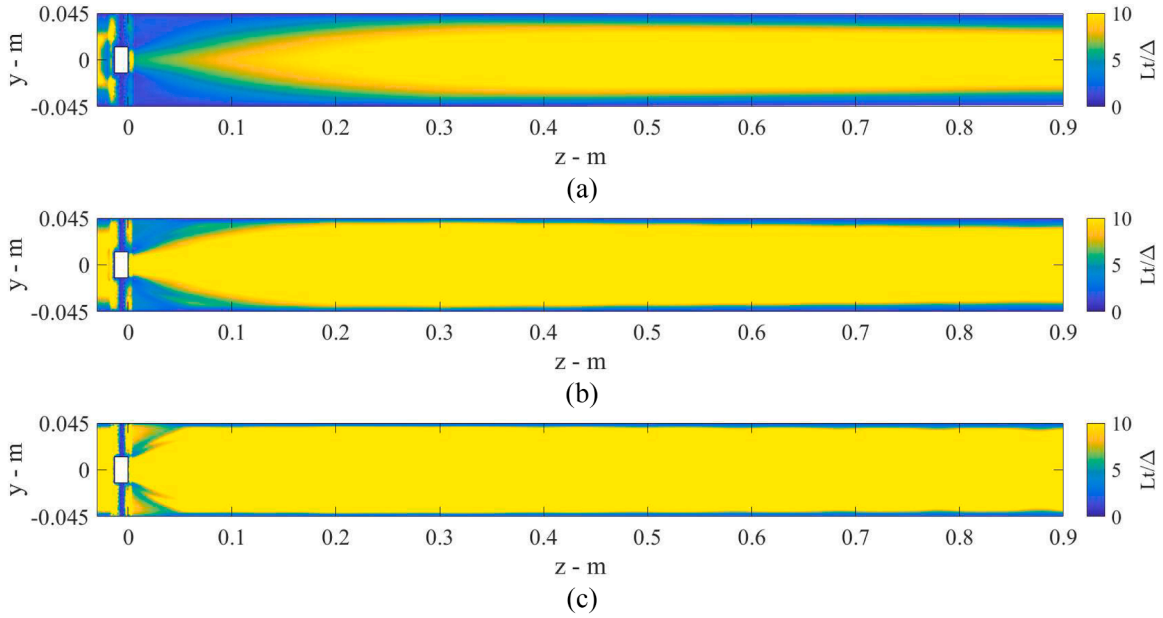

Fig. 2. Estimate of the integral length scale to mesh size ratio, $\boldsymbol{Lt/\Delta}$, on a vertical plane passing through the pipe axis (hub shown in white) obtained from RANS simulations by adopting the coarsest grid, (a), the intermediate grid, (b) and the finest grid (c). The pipe section upstream the swirler is cropped to improve readability.

DES approach operating in LES mode to resolve the large flow structures, especially in the zone immediately downstream the swirler. While both the intermediate, Fig. 2b, and finest, Fig. 2c, meshes have a sufficient resolution for the LES to capture the majority of the large eddies, the finest mesh is expected to better capture the flow structures downstream the swirler, and therefore it was selected for the study.

Fig. 3 shows the time average DES turbulent kinetic energy dissipation multiplier, Eq. (20), as obtained from the single-phase detached eddy simulation with the finest grid.

As stated in Section 3.2, f_d approaches unity away from the walls, where the DES operates in LES mode. Therefore Fig. 3 shows the portion of the domain operating in LES mode, RANS mode and a blending of the two approaches with the DES adopting the finest grid. Fig. 3 shows that the majority of the volume downstream of the swirler is solved in LES mode, and this portion accounts for 78.8 % of the pipe volume.

The convergence study also highlighted that with the finest mesh the turbulent dissipation rate in the volume downstream of the swirler as predicted by the RANS simulations was underpredicted by around 10 %, and by around 14 % with the DES simulations, with respect to the corresponding Richardson extrapolations calculated on three grids.

4.2. Boundary and initial conditions, numerical schemes and convergence criteria

The set of equations of the numerical model presented in Section 3 was numerically solved inside the discretized geometry presented in Section 4.1. For both simulation approaches, no-slip boundary conditions were enforced at the solid walls for the gas and liquid phases, the inlet conditions corresponded to a velocity inlet, in which just the mean velocity was defined. In fact, the long pipe section before the swirler allowed for the flow field to fully develop, therefore no synthetic turbulence generation was adopted at the inlet for the DES simulations. The pipe outlet was modeled as a pressure outlet with zero-gauge pressure.

The numerical schemes employed for the solution of the model equations are reported in Table 1. A second order implicit time scheme was used, with a time step equal to 0.5 ms, corresponding to a maximum Courant number of around 2.0. The numerical schemes adopted for the RANS and DES simulations were the same, except for the discretization of the divergence of the velocity, for which a II order UPWIND scheme and a bounded central-difference scheme were selected for the RANS and DES simulations, respectively.

A decoupled solution of the PBE and the flow equations was performed for both the RANS and DES simulations to obtain information on the BSD. The converged gas–liquid flow field obtained with a constant bubble size equal to 1.4 mm was used as initial condition for the solution of the PBE and the same bubble size was considered to obtain the NDF

Table 1
Numerical schemes for the numerical solutions

Variable	Scheme
Time	Second order implicit
Gradients	Least squares cell based
Diffusive terms	Central-difference
$\nabla\cdot\boldsymbol{u}$	II order UPWIND (RANS)
	Bounded central-difference (DES)
$\nabla\cdot\boldsymbol{\varphi}$	II order UPWIND
NDF moment	I order UPWIND
Pressure interpolation	PRESTO!

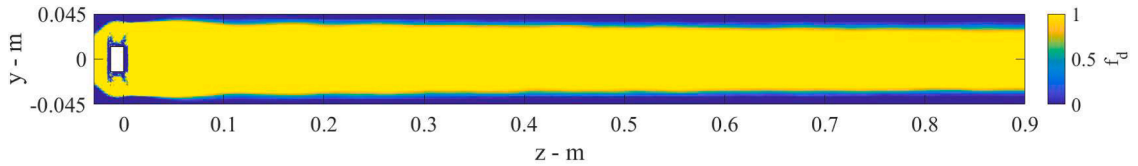

Fig. 3. Time average DES turbulent kinetic energy dissipation multiplier, f_d, on a vertical plane passing through the pipe axis (hub shown in white) obtained from DES with the finest grid. The pipe section upstream the swirler is cropped to improve readability.

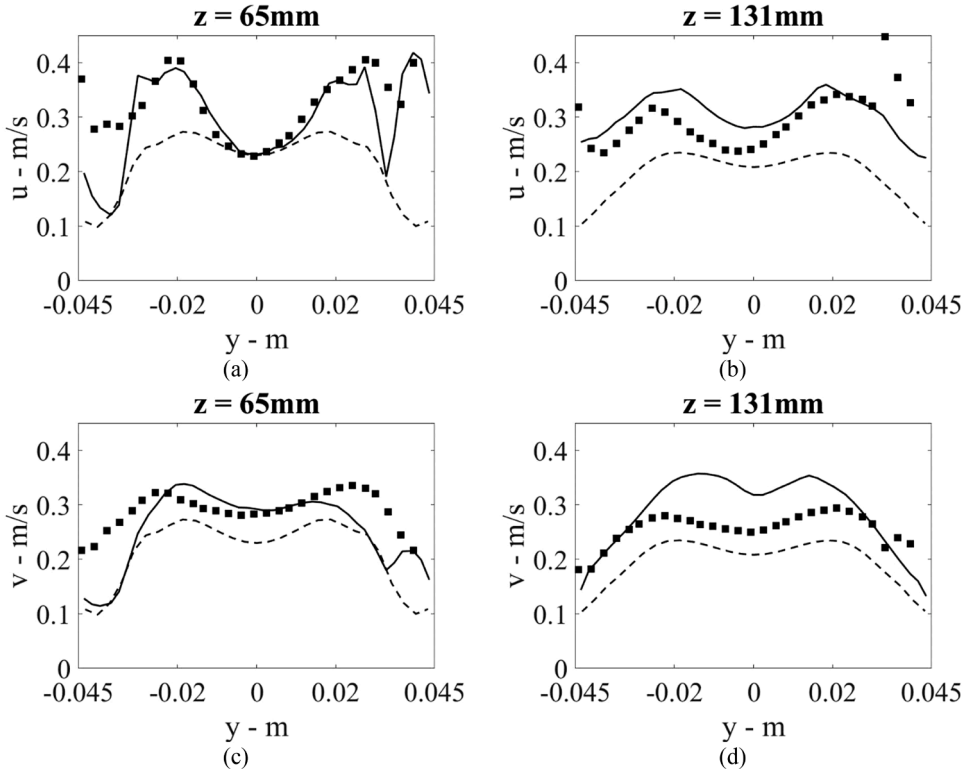

Fig. 4. Profiles of time averaged axial velocity fluctuations, u (a and b), and y-velocity fluctuations, v (c and d), along the y-coordinate at different axial positions as obtained from experiments, squares, from DES simulations, solid lines, and from RANS simulations, dashed lines.

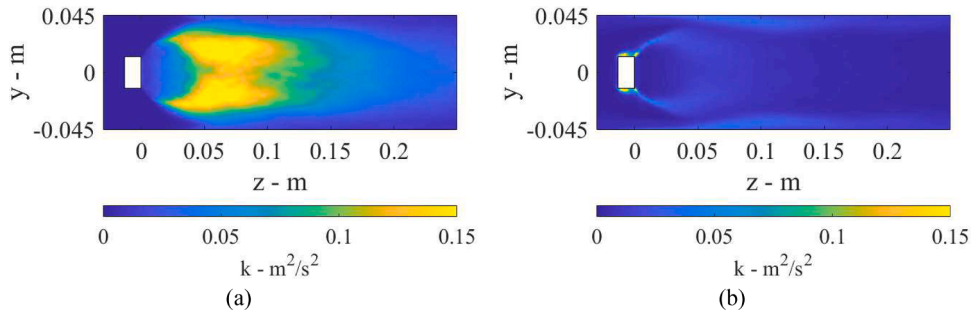

Fig. 5. Time averaged resolved (a) and modeled (b) turbulent kinetic energy on a vertical plane passing through the pipe axis in the proximity of the swirler (hub shown in white), as predicted by the DES.

moments at the inlet. The value of the bubble diameter was taken from experimental observations (Maluta et al., 2023).

Convergence was assumed once the total moment on the solid walls, calculated as the sum of the area integral of the pressure and viscous forces with the pipe centre as the moment axis, reached a plateau, and the moment fluctuations were lower than 0.1 % of the final value. Additionally, it was ensured that convergence was reached when the variation of the volume fraction inside the system, the overall pressure drop and the integral of the turbulent dissipation rate were lower than 2.0 % of their respective final value obtained from each simulation. An average window of 2.4 s was identified, based on a sensitivity analysis, and the mean velocity, the mean velocity components and the mean turbulent kinetic energy were monitored on six locations downstream of the swirler, ensuring that their mean value did not change once convergence was reached.

5. Results

5.1. Single-phase simulations

The single-phase fluid dynamics of the system was analyzed to validate the modeling approach. The time averaged fluctuating velocity axial components along the y-coordinate, with the axis center positioned in the center of the swirler hub face towards the outlet, the z-axis parallel to the pipe axis and the y-axis pointing up, were compared with experimental data. The results are shown in Fig. 4.

In Fig. 4, the velocity fluctuations for the RANS simulations were obtained from the value of turbulent kinetic energy, k, as:

$$u = v = \sqrt{\frac{2}{3}k} \tag{29}$$

While for the DES simulation the root mean square of the velocity components averaged on a 2.4 s window were considered, increased by the sub-grid-scale fluctuating contribution obtained with Eq. (29), in which k was changed to its sub-grid value averaged on the same 2.4 s window.

Fig. 4 shows that a relatively good agreement with the experimental data was obtained with the DES simulation. The deviations from the experimental data are generally larger towards the walls of the pipe, where the DES turbulence model transitions to the realizable $k-\varepsilon$ turbulence model of the RANS formulation, as shown in Section 4.1. The only exception to this behavior is found in the y-velocity fluctuations at high axial coordinate, Fig. 4d, where the maximum deviation from the experimental data is close to 35 %, and it is found towards the centre of the pipe, at $y = -0.011$ m. This deviation observed with the DES is still smaller than the maximum deviations from the experiments observed with the RANS approach, therefore it can be concluded that the DES improves the agreement with the experimental data obtainable with pure RANS simulations. In fact, in addition to the larger deviations from experimental data, the two-equation realizable $k-\varepsilon$ turbulence model adopted in the RANS simulations cannot intrinsically replicate the different profiles between different fluctuating components observed in the experiments. Theoretical considerations state that models exploiting Boussinesq approximation for eddy viscosity cannot predict anisotropic velocity fluctuations, therefore the predictive capabilities of such models in nonstandard flows must be verified with experimental results. In fact, in a previous work (Maluta et al., 2023) it was observed that two-equations turbulence models outperformed the RSM, in the system under study, and the direct solution of some of the turbulence scales evidences the improvement in the flow predictions.

Concerning the DES approach, to quantify the contribution of the resolved and modeled portion of the velocity fluctuations on the total, the time averaged sub-grid scale and the time averaged resolved turbulent kinetic energy were compared, and they are shown in Fig. 5.

Fig. 5 clearly shows that downstream in the proximity of the swirler the largest contribution to the turbulent kinetic energy is resolved, Fig. 5a, rather than modeled, Fig. 5b. The volume averaged resolved turbulent kinetic energy in the downstream section of the pipe is equal to 1.93×10^{-2} m^2/s^2, and the volume averaged modeled part in the same section is equal to 6.30×10^{-3} m^2/s^2, thus highlighting that more than 75 % of the total turbulent kinetic energy is resolved by the DES approach.

The concentrated pressure drop, ΔP, due to the swirler was calculated as the difference between two vertical sections just upstream and just downstream the inline separator, and it was compared with the experimental measurement of 1005 Pa (Maluta et al., 2023). The results are shown in Table 2, together with the deviation from the experimental value, ΔExp.

Consistently to what previously found with different RANS turbulence models, the pressure drop is slightly underestimated, with respect to the experimental value, by less than 15 %. It is interesting to highlight that the DES approach improves the agreement with the experimental result, compared with the RANS simulation.

Table 2
Pressure drop values due to the swirler and deviations from the experimental measurement.

Model approach	ΔP – Pa	ΔExp
RANS	863	14.1 %
DES	894	10.9 %

5.2. Gas–liquid simulations

The swirler separates the gas from the liquid by providing a tangential component to the fluids in the pipe. Due to the different densities, the lighter phase accumulates towards the centre of the pipe. The results of the gas–liquid simulations obtained with a constant bubble size equal to 1.4 mm derived from the experimental observation are reported in this section. The time averaged gas volume fraction distribution on a vertical plane passing through the pipe axis as predicted by the two different turbulence models are reported in Fig. 6.

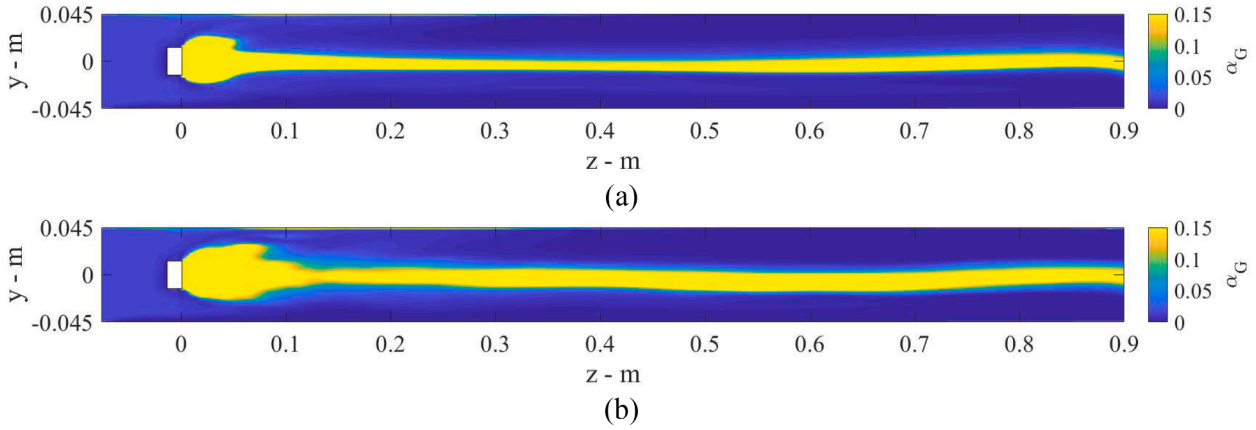

Fig. 6. Time averaged gas volume fraction distribution on a vertical plane passing through the pipe axis (hub shown in white), as predicted by the RANS (a) and DES (b) simulations. The pipe section upstream the swirler is cropped to improve readability.

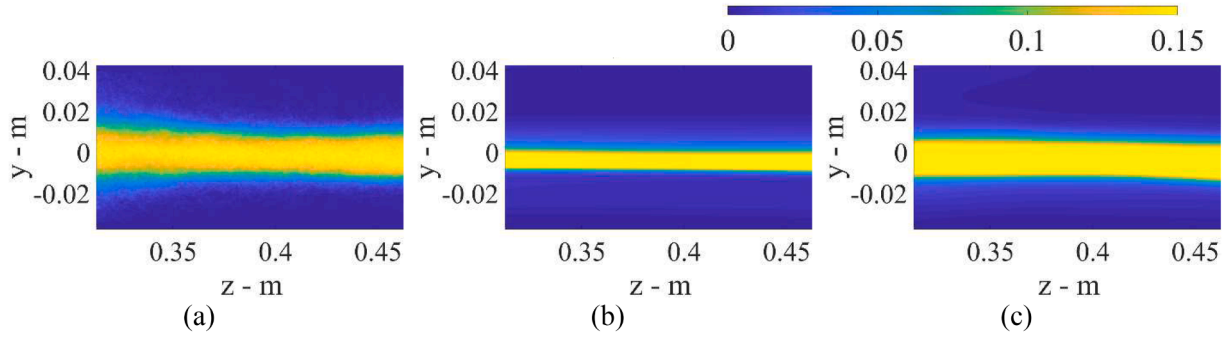

Fig. 7. Time averaged gas volume fraction on a vertical plane passing through the pipe axis as experimentally measured (a) and obtained with the RANS (b) and DES (c) approaches. The legend on the top refers to Fig. (b) and (c) only.

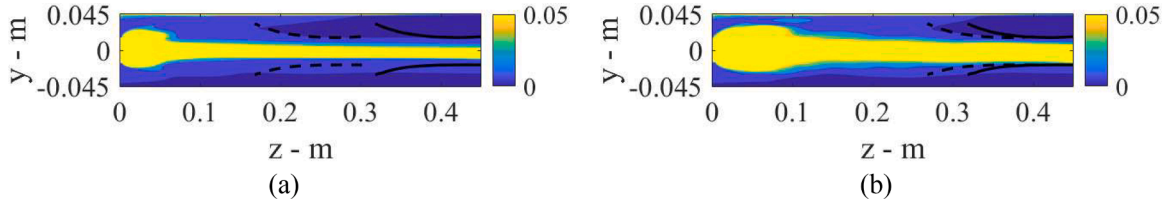

Fig. 8. Time averaged gas volume fraction distribution on a portion of a vertical plane passing through the pipe axis downstream of the swirler. The experimentally determined edges of the conical zone of gas accumulation are reported as black lines on the RANS (a) and DES (b) predictions. The solid lines show the experimental position on the cone, while its shifted position to match the CFD predictions are shown as dashed lines.

Fig. 6 shows that the experimentally observed change in the gas volume fraction distribution from the pipe section upstream the swirler and the one downstream the swirler is well captured by both the simulation approaches. The gas accumulation towards the center of the pipe is consistently observed up to 10 pipe diameters, which is the limit of the computational domain, and in both cases two distinct gas accumulation zones are predicted, one closer to the swirler and one further away. These two zones are also experimentally observed and they are called the conical and the cylindrical central core of gas accumulation, respectively (Maluta et al., 2023). The qualitative behavior of the gas–liquid mixture flowing in the pipe with the compact inline separator is well captured by both the simulation approaches, and in the following, the quantitative analysis of the conical and cylindrical zone of gas accumulation are presented.

Starting from the experimental observation of a portion of pipe with axial coordinates between 0.31 m $< z <$ 0.46 m, the shape and size of the central zone of gas accumulation was determined. The experimental color scale was obtained from the pipe portion corresponding to just liquid and the zones with high gas hold up, and the pixel intensities were normalized between 0 to 1 (Maluta et al., 2023). From the experimental results it was not possible to correlate the pixel intensities to gas hold-up. It is worth mentioning that towards the pipe axis large gas volume fraction gradients are observable, and it was observed that the numerical results are fairly insensitive to the color scale adopted. Time averaged gas volume fraction distributions in the zone experimentally observed were collected from the results of the RANS and DES simulations, and the results are shown in Fig. 7.

The experimental gas distribution in Fig. 7a shows that a cylinder with high gas volume fraction is present towards the centre of the pipe of the sampled zone. Moreover, low gas volume fractions surround this central cylinder, forming a cone at axial coordinates lower than about 0.35 m, and transitioning to a cylinder at higher axial coordinates.

Concerning the conical zone of gas accumulation, its axial position is underestimated by both simulation approaches, as it can be seen from

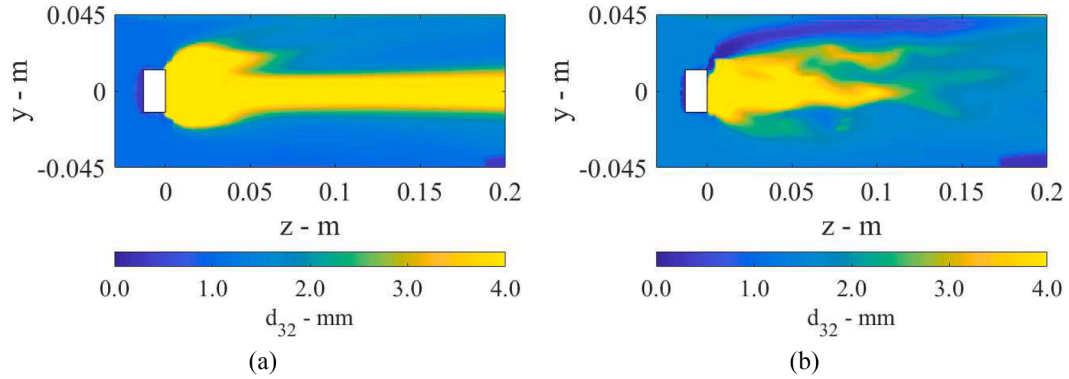

Fig. 9. Sauter mean diameter on a vertical plane passing through the pipe axis in the proximity of the swirler (hub shown in white), as predicted by the RANS, (a) and DES, (b), approach.

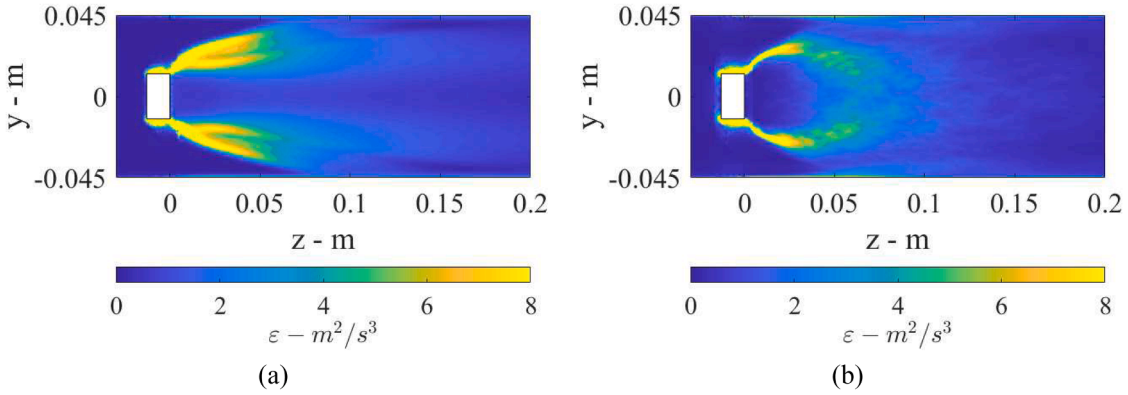

Fig. 10. Time averaged turbulent dissipation rate on a vertical plane passing through the pipe axis in the proximity of the swirler (hub shown in white), as predicted by the RANS, (a) and DES, (b), approach.

the time averaged gas volume fraction distributions in Fig. 8.

Fig. 8 shows the downstream pipe section, where the experimentally determined edges of the conical zone of gas accumulation are reported as black lines. The solid lines indicate the shape and the axial position of the experimental conical zone of gas accumulation which was identified with a white hue threshold of 0.1, while the threshold to obtain the numerical edge of the zones of gas accumulations was identified with gas volume fraction value of 0.01 (Maluta et al., 2023). It can be seen that the RANS simulation, Fig. 8a, underpredicts the axial position by around 150 mm, while the DES approach, Fig. 8b, underpredicts it by 50 mm. Once again, the DES improves the agreement with the experimental data with respect to the RANS simulations, since the DES underprediction of the axial coordinate of the conical zone is around half pipe diameter, while the RANS underprediction is larger than 1.6 pipe diameters. Interestingly, the shape of the upper portion of the conical edge is satisfactorily predicted by both simulation approaches, while the lower portion is not. This behavior is likely related to having used a constant bubble size in the gas–liquid simulations. In fact, large bubbles generated by coalescence phenomena would float faster towards the upper edge of the pipe, with respect to the small bubbles generated from the passage of the mixture through the swirler blades. Since a constant bubble size is adopted, downstream of the swirler bubbles can travel longer paths in the proximity of the pipe centre, with respect to what experimentally observed.

To limit the bias in the analysis of the gas-volume fraction maps in Figs. 6–8, and to make the comparison consistent with previous investigations, the range of the colormaps, and the experimental and numerical gas accumulation extension thresholds were assumed equal to those previously identified for a similar system where a comparison with Two-Fluids Model RANS simulations (Maluta et al., 2023) was performed.

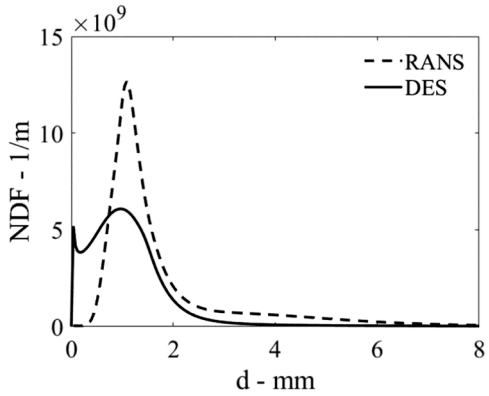

Fig. 11. Volume averaged number density function in the volume downstream of the swirler as predicted by the RANS and DES approaches

A discussion on the bubble size distribution obtainable through the solution of a PBE is presented in the following section.

5.3. Decoupled solution of the population balance equation

In this section the results of the solution of the PBE presented in Section 3.3 are presented. The results are obtained by decoupling the PBE solution from the fluid flow equations. In this way the moments of the NDF are transported through the moment transform of Eq. (21), but the flow field is not affected by the bubble size. The converged time

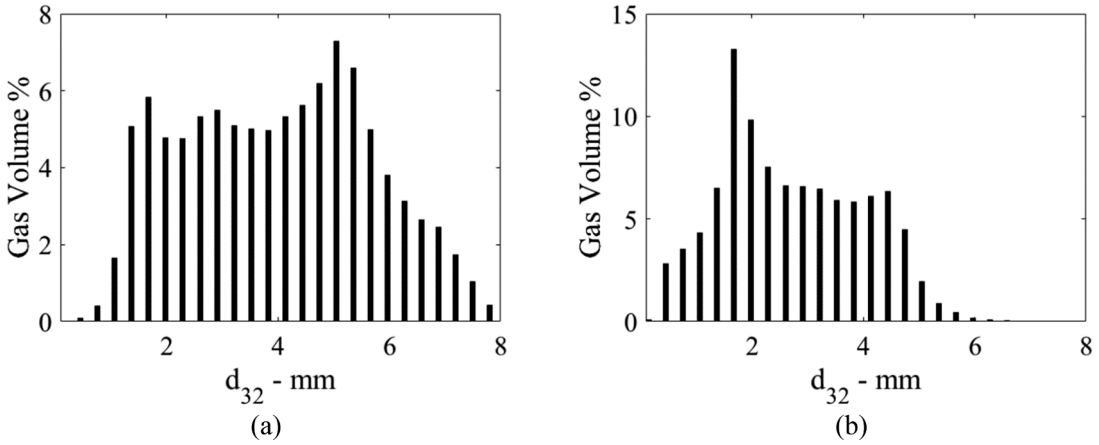

Fig. 12. Sauter mean bubble size distribution in the pipe volume downstream the swirler, as predicted by the RANS, a, and DES, b, approaches.

average flow variables are adopted in the PBE solution, to obtain preliminary information on the distribution of bubble mean diameters. The spatial distributions of two characteristic bubble sizes were considered, namely the arithmetic mean, d_{10}, and the Sauter mean, d_{32}, bubble diameter. Both these characteristic sizes are readily obtained from the local transported moments of the number density function as:

$$d_{10} = M_1/M_0 \tag{30}$$

$$d_{32} = M_3/M_2 \tag{31}$$

The spatial distribution of the local d_{32} obtained with the two simulation approaches is reported in Fig. 9.

Fig. 9 shows that large bubbles are accumulating in the wake of the swirler towards the pipe axis. The main difference between the two modeling approaches is in the Sauter mean diameter in the central zone of gas accumulation. In fact, in the RANS simulation, Fig. 9a, d_{32} higher than 4.0 mm are found all along the gas accumulation zone towards the centre of the pipe, while in the same zone, the DES, Fig. 9b, predicts d_{32} higher than 4.0 mm just up to an axial coordinate around 0.1 m. The reason for this difference may be related to the different turbulent dissipation rate distributions obtained from the two different approaches, as shown in Fig. 10.

Fig. 10 shows that similar turbulent dissipation rate intensities are predicted by both simulation approaches downstream of the swirler, in fact, the mass integrals of the turbulent dissipation rate on the pipe volume downstream of the swirler are similar and equal to 3.26 W and 3.14 W for the RANS and DES, respectively. Conversely, the spatial distribution of turbulent dissipation rate between $0.05 < z < 0.1$ shows that towards the centre of the pipe higher turbulent dissipation rate is predicted by the DES, Fig. 10b, with respect to the RANS simulation, Fig. 10a. The pipe axis is where most of the gas is accumulated, therefore smaller bubble sizes are produced in the proximity of the swirler by the DES, compared with the RANS, due to the enhanced breakup events. The resulting NDF is then subsequently advected along the central zone of gas accumulation, propagating the moments corresponding to the NDF subject to high breakup rates. On the other hand, RANS simulations predict smaller values of ε towards the pipe center, leading to a lower breakup rate which results in the advection of the NDF moments corresponding to larger bubbles along the central zone of gas accumulation. The analysis of the turbulent dissipation rate distribution effects on the predicted BSD in such inline swirler separation processes stems for the results obtained in different systems (Chen et al., 2020; Maluta et al., 2021). Additional study must be directed to the validation of the population balance modeling in the system under consideration, also analyzing the bubble-bubble interactions (Gimbun et al., 2016) and the effect of the whole turbulence spectrum on the predictions (Niño et al., 2020).

Table 3
Characteristic mean bubble diameters as predicted by the two simulation approaches

Model approach	d_{10} - mm	d_{32} - mm
RANS	1.50	3.90
DES	1.13	3.15

To further analyze the different bubble size distributions predicted by the two modeling approaches, the volume averaged number density function in the volume downstream of the swirler is shown in Fig. 11.

The BSDs shown in Fig. 11 were locally reconstructed with the Extended Quadrature Method Of Moments, EQMOM (Marchisio and Fox, 2013), approximating each BSD with a sum of lognormal distributions. The local reconstructed BSD were phase averaged in the volume downstream of the swirler. Both the phase averaged distributions have a peak around 1 mm, but the RANS simulation predicts fewer bubbles below this threshold, with respect to the DES simulation. On the contrary, while the number of bubbles with diameter larger than 1 mm rapidly decreases with both approaches, the RANS simulation predicts larger bubbles than the DES simulation. Thus, the DES simulation predicts a narrower bubble size distributions shifted towards smaller diameters.

Since these results are volume averaged, information regarding the local population of the bubbles is lost. For this reason, the local distributions of the Sauter mean diameter, which is the bubble size used to calculate the interphase forces, are also reported in terms of gas volume distributions in the pipe volume downstream of the swirler and they are shown in Fig. 12.

Fig. 12 shows that in the volume downstream of the swirler the distribution of the local Sauter mean diameters spans more than one order of magnitude. In particular, the RANS simulations, Fig. 12a, predict that the local distributions of bubbles with d_{32} between 2.5 mm and 7.0 mm account for around 75 % of the gas volume, while DES, Fig. 12b, predicts that in the same gas volume percent the local distributions of bubbles have d_{32} from 1.7 mm to 4.6 mm. Moreover, the local d_{32} distributions in the volume downstream of the swirler confirm what observed for the NDFs in Fig. 11, which is that the DES simulation predicts a narrower bubble size distribution shifted towards smaller diameters, with respect to the RANS simulation. In the experiments, the bubble size distribution was obtained on a vertical plane with an axial extension from 0.45 m to 0.56 m and a radial extension from 0.02 m to 0.04 m, and a d_{10} equal to 1.4 mm was found (Maluta et al., 2023). The arithmetic and the Sauter mean bubble diameters were calculated for both the simulation approaches in the same pipe portion as the experimental campaign, and the results are reported in Table 3.

Table 3 shows that smaller characteristic diameters are obtained from the DES, consistently to what observed in Fig. 12. A comparison with the experimental data is not relevant since the bubble size results were obtained by decoupling the solution of the PBE and the equations of the fluid flow. Nonetheless, this analysis shows that smaller diameters are predicted by the DES compared to the RANS simulation, even though very similar integrals of the turbulent dissipation rates are obtained.

6. Conclusions

A compact inline swirling generating device for the separation of gas–liquid mixtures was numerically simulated with Reynolds averaged Navier–Stokes and a detached eddy simulation approach. Based on the quantitative comparison with experimental data in single-phase and qualitative gas–liquid experimental observations, this study shows that the DES approach improves the agreement with the experimental data, compared with RANS predictions.

In fact, results concerning the single-phase simulation of the liquid flow field show that the turbulent fluctuations of the velocity components and the pressure drop due to the swirler as predicted by the DES have smaller deviations from the experimental results than the predictions of the RANS simulations.

Concerning the gas–liquid results, although both simulation approaches correctly qualitatively predict the gas accumulation downstream of the swirler, the size of the cylindrical zone of gas accumulation and the axial position of the boundaries of the conical zone of gas accumulation as predicted by the DES approach are in better agreement with the experimental observations. These results depend on the choice of the local gas volume fraction thresholds, which were taken from the literature to minimize the bias in the analysis and to make the comparison consistent with previous investigations.

The analysis of the turbulent field shows that important differences are observable in the local distribution of turbulent dissipation rate, which affect the prediction of the population balance equation. The importance of this finding will be further studied, since the accurate prediction of the region of maximum turbulent dissipation rate may improve the development of breakup and coalescence kernels, and lead to the formulation of grid independent PBE kernels, as done for stirred tanks.

Overall, the detached eddy simulation proved to be exploitable in the numerical modeling of process equipment, leading to improved predictions of the gas–liquid flow field, with respect to the RANS approach.

CRediT authorship contribution statement

Francesco Maluta: Conceptualization, Writing – original draft, Methodology, Formal analysis. **Alessandro Paglianti:** Conceptualization, Writing – original draft, Supervision, Validation. **Giuseppina Montante:** Conceptualization, Writing – original draft, Supervision, Investigation.

Declaration of Competing Interest

The authors declare that they have no known competing financial interests or personal relationships that could have appeared to influence the work reported in this paper.

Data availability

Data will be made available on request.

References

Bird, R.B., Stewart, W.E., Lightfoot, E.N., 1960. Transport Phenomena. Wiley & Sons, Inc., New York.

Brown, G.J., Fletcher, D.F., Leggoe, J.W., Whyte, D.S., 2020. Application of hybrid RANS-LES models to the prediction of flow behaviour in an industrial crystalliser. Appl. Math. Model. 77, 1797–1819. https://doi.org/10.1016/J.APM.2019.09.032.

Buffo, A., Vanni, M., Marchisio, D.L., 2016. On the implementation of moment transport equations in OpenFOAM: Boundedness and realizability. Int. J. Multiph. Flow 85, 223–235. https://doi.org/10.1016/j.ijmultiphaseflow.2016.06.017.

Cai, B., Wang, J., Sun, L., Zhang, N., Yan, C., 2014. Experimental study and numerical optimization on a vane-type separator for bubble separation in TMSR. Prog. Nucl. Energy 74, 1–13. https://doi.org/10.1016/j.pnucene.2014.02.007.

Chen, Y., Ding, J., Weng, P., Yang, X., Wu, W., 2020. On the breakup of Taylor length scale size bubbles and droplets in turbulent dispersions. Chem. Eng. J. 386, 121826 https://doi.org/10.1016/j.cej.2019.05.187.

Coroneo, M., Montante, G., Paglianti, A., 2012. Computational fluid dynamics modeling of corrugated static mixers for turbulent applications. Ind. Eng. Chem. Res. 51, 15986–15996. https://doi.org/10.1021/ie300398z.

Deen, N.G., Solberg, T., Hjertager, B.H., 2001. Large eddy simulation of the gas–liquid flow in a square cross-sectioned bubble column. Chem. Eng. Sci. 56, 6341–6349. https://doi.org/10.1016/S0009-2509(01)00249-4.

Derksen, J.J., Van Den Akker, H.E.A., Sundaresan, S., 2008. Two-way coupled large-eddy simulations of the gas-solid flow in cyclone separators. AIChE J. 54, 872–885. https://doi.org/10.1002/AIC.11418.

Dhotre, M.T., Deen, N.G., Niceno, B., Khan, Z., Joshi, J.B., 2013. Large eddy simulation for dispersed bubbly flows: a review. Int. J. Chem. Eng. https://doi.org/10.1155/2013/343276.

Falzone, S., Buffo, A., Vanni, M., Marchisio, D.L., 2018. Simulation of Turbulent Coalescence and Breakage of Bubbles and Droplets in the Presence of Surfactants, Salts, and Contaminants, in: Advances in Chemical Engineering. Academic Press Inc., pp. 125–188. https://doi.org/10.1016/bs.ache.2018.01.002

Gimbun, J., Liew, S.Y., Nagy, Z.K., Rielly, C.D., 2016. Three-way coupling simulation of a gas–liquid stirred tank using a multi-compartment population balance model. Chem. Prod. Process Model. 11, 205–216. https://doi.org/10.1515/cppm-2015-0076.

Gimbun, J., Rielly, C.D., Nagy, Z.K., Derksen, J.J., 2012. Detached eddy simulation on the turbulent flow in a stirred tank. AIChE J. 58, 3224–3241. https://doi.org/10.1002/AIC.12807.

Green, D.W., Perry, R.H., 2008. Perry's Chemical Engineers' Handbook, 8th Ed. McGraw-Hill.

Guha, D., Ramachandran, P.A., Dudukovic, M.P., Derksen, J.J., 2008. Evaluation of large Eddy simulation and Euler-Euler CFD models for solids flow dynamics in a stirred tank reactor. AIChE J. 54, 766–778. https://doi.org/10.1002/AIC.11417.

Ishii, M., Zuber, N., 1979. Drag coefficient and relative velocity in bubbly, droplet or particulate flows. AIChE J. 25, 843–855. https://doi.org/10.1002/aic.690250513.

Kader, B.A., 1981. Temperature and concentration profiles in fully turbulent boundary layers. Int. J. Heat Mass Transf. 24, 1541–1544. https://doi.org/10.1016/0017-9310(81)90220-9.

Kharoua, N., Khezzar, L., Alshehhi, M., 2018. The interaction of confined swirling flow with a conical bluff body: Numerical simulation. Chem. Eng. Res. Des. 136, 207–218. https://doi.org/10.1016/J.CHERD.2018.04.034.

Kouzbour, S., Maniscalco, F., Buffo, A., Vanni, M., Grau, F.X., Gourich, B., Stiriba, Y., 2023. Effects of SDS surface-active agents on hydrodynamics and oxygen mass transfer in a square bubble column reactor: experimental and CFD modeling study. Int. J. Multiph. Flow 165, 104486. https://doi.org/10.1016/J.IJMULTIPHASEFLOW.2023.104486.

Luo, H., Svendsen, H.F., 1996. Theoretical model for drop and bubble breakup in turbulent dispersions. AIChE J. 42, 1225–1233. https://doi.org/10.1002/aic.690420505.

Lyras, T., Karathanassis, I.K., Kyriazis, N., Koukouvinis, P., Gavaises, M., 2021. Modelling of liquid oxygen nozzle flows under subcritical and supercritical pressure conditions. Int. J. Heat Mass Transf. 177, 121559 https://doi.org/10.1016/j.ijheatmasstransfer.2021.121559.

Ma, J., Oberai, A.A., Lahey, R.T., Drew, D.A., 2011. Modeling air entrainment and transport in a hydraulic jump using two-fluid RANS and DES turbulence models. Heat Mass Transf. 47, 911–919. https://doi.org/10.1007/s00231-011-0867-8.

Maluta, F., Buffo, A., Marchisio, D., Montante, G., Paglianti, A., Vanni, M., 2021. Effect of turbulent kinetic energy dissipation rate on the prediction of droplet size distribution in stirred tanks. Int. J. Multiph. Flow 136, 103547. https://doi.org/10.1016/j.ijmultiphaseflow.2020.103547.

Maluta, F., Paglianti, A., Montante, G., 2023. Experimental and numerical study of a compact inline swirler for gas–liquid separation. Chem. Eng. Sci. 265, 118219 https://doi.org/10.1016/j.ces.2022.118219.

Manninen, M., Taivassalo, V., Kallio, S., 1996. On the mixture model for multiphase flow. VTT Publications. Technical Research Centre of Finland, Espoo (Finland).

Marchisio, D.L., Fox, R.O., 2013. Computational Models for Polydisperse Particulate and Multiphase Systems. Cambridge University Press, Cambridge. https://doi.org/10.1017/CBO9781139016599.

Marshall, E.M., Bakker, A., 2004. Computational fluid mixing. In: Paul, E.L., Atiemo-Obeng, V.A., Kresta, S.M. (Eds.), Handbook of Industrial Mixing Science and Practice. John Wiley & Sons Inc., Hoboken, New Jersey, USA.

Masood, R.M.A., Delgado, A., 2014. Numerical investigation of three-dimensional bubble column flows: a detached Eddy simulation approach. Chem. Eng. Technol. 37, 1697–1704. https://doi.org/10.1002/ceat.201400173.

Masterov, M.V., Baltussen, M.W., Kuipers, J.A.M., 2018. Numerical simulation of a square bubble column using detached Eddy simulation and Euler–Lagrange approach. Int. J. Multiph. Flow 107, 275–288. https://doi.org/10.1016/j.ijmultiphaseflow.2018.06.006.

Niño, L., Gelves, R., Ali, H., Solsvik, J., Jakobsen, H., 2020. Applicability of a modified breakage and coalescence model based on the complete turbulence spectrum

concept for CFD simulation of gas–liquid mass transfer in a stirred tank reactor. Chem. Eng. Sci. 211, 115272 https://doi.org/10.1016/j.ces.2019.115272.
Prince, M.J., Blanch, H.W., 1990. Bubble coalescence and break-up in air-sparged bubble columns. AIChE J. 36, 1485–1499. https://doi.org/10.1002/aic.690361004.
Putra, R.A., Schäfer, T., Neumann, M., Lucas, D., 2018. CFD studies on the gas–liquid flow in the swirl generating device. Nucl. Eng. Des. 332, 213–225. https://doi.org/10.1016/j.nucengdes.2018.03.034.
Shaban, H., Tavoularis, S., 2018. Detached eddy simulations of rising Taylor bubbles. Int. J. Multiph. Flow 107, 289–300. https://doi.org/10.1016/j.ijmultiphaseflow.2018.06.008.
Shih, T.-H., Liou, W.W., Shabbir, A., Yang, Z., Zhu, J., 1995. A new k-ϵ eddy viscosity model for high reynolds number turbulent flows. Comput. Fluid. 24, 227–238. https://doi.org/10.1016/0045-7930(94)00032-T.
Song, J., Kharoua, N., Khezzar, L., Alshehhi, M., 2021. Numerical simulation of turbulent swirling pipe flow with an internal conical bluff body. Fluid Dyn. Mater. Process. 17, 455–470. https://doi.org/10.32604/FDMP.2021.014370.
Spalart, P.R., Deck, S., Shur, M.L., Squires, K.D., Strelets, M.K., Travin, A., 2006. A new version of detached-Eddy simulation, resistant to ambiguous grid densities. Theor. Comput. Fluid Dyn. 20, 181–195. https://doi.org/10.1007/s00162-006-0015-0.
Stankiewicz, A.I., Moulijn, J.A., 2000. Process intensification: Transforming chemical engineering. Chem. Eng. Prog. 96, 22–33.
Versteeg, H., Malalasekera, W., 2007. An Introduction to Computational Fluid Dynamics - The Finite Volume Method, 2nd ed. Pearson Education Limited, Harlow, England (UK).
Wang, Y., Politano, M., Weber, L., 2019. Spillway jet regime and total dissolved gas prediction with a multiphase flow model. J. Hydraul. Res. 57, 26–38. https://doi.org/10.1080/00221686.2018.1428231.
Yin, J., Ma, Y., Qian, Y., Wang, D., 2016. Experimental investigation of the bubble separation route for an axial gas–liquid separator for TMSR. Ann. Nucl. Energy 97, 1–6. https://doi.org/10.1016/j.anucene.2016.06.018.
Yuan, F., Cui, Z., Lin, J., 2020. Experimental and numerical study on flow resistance and bubble transport in a helical static mixer. Energies 13, 1228. https://doi.org/10.3390/en13051228.
Zhang, Z., Liao, R., Cai, Z., Liu, J., 2020. An orthogonal numerical simulation experiment study towards the decay characteristics and effective swirl length of the swirling flow in a vortex tool inserted tube. J. Nat. Gas Sci. Eng. 76, 103220 https://doi.org/10.1016/j.jngse.2020.103220.
Zidouni, F., Krepper, E., Rzehak, R., Rabha, S., Schubert, M., Hampel, U., 2015. Simulation of gas–liquid flow in a helical static mixer. Chem. Eng. Sci. 137, 476–486. https://doi.org/10.1016/j.ces.2015.06.052.